

# Photothermoacoustic imaging of biological tissues: maximum depth characterization comparison of time and frequency-domain measurements

Sergey A. Telenkov  
Andreas Mandelis

University of Toronto  
Center for Advanced Diffusion-Wave Technologies  
Department of Mechanical and Industrial Engineering  
5 King's College Road  
Toronto, Ontario M5S 3G8  
Canada

**Abstract.** The photothermoacoustic (PTA) or photoacoustic (PA) effect induced in light-absorbing materials can be observed either as a transient signal in time domain or as a periodic response to modulated optical excitation. Both techniques can be utilized for creating an image of subsurface light-absorbing structures (chromophores). In biological materials, the optical contrast information can be related to physiological activity and chemical composition of a test specimen. The present study compares experimentally the two PA imaging modalities with respect to the maximum imaging depth achieved in scattering media with optical properties similar to biological tissues. Depth profilometric measurements were carried out using a dual-mode laser system and a set of aqueous light-scattering solutions mimicking photon propagation in tissue. Various detection schemes and signal processing methods were tested to characterize the depth sensitivity of PA measurements. The obtained results demonstrate the capabilities of both techniques and can be used in specific PTA imaging applications for development of image reconstruction algorithms aimed at maximizing system performance. Our results demonstrate that submillimeter-resolution depth-selective PA imaging can be achieved without nanosecond-pulsed laser systems by appropriate modulation of a continuous laser source and a signal processing algorithm adapted to specific parameters of the PA response. © 2009 Society of Photo-Optical Instrumentation Engineers. [DOI: 10.1117/1.3200924]

Keywords: photoacoustics; lasers in medicine; ultrasonics; imaging; fourier transforms; tissues.

Paper 09094R received Mar. 19, 2009; revised manuscript received May 25, 2009; accepted for publication Jun. 15, 2009; published online Aug. 7, 2009.

## 1 Introduction

The photoacoustic (PA) response of biological tissues to optical irradiation has been actively studied with the ultimate goal of developing a noninvasive imaging modality capable of providing information on optical heterogeneities at depths greatly exceeding those accessible by purely optical means.<sup>1-4</sup> Owing to the fact that at optical excitation levels below the vaporization and ablation thresholds, acoustic wave generation is associated with thermoelastic deformations, the term photothermoacoustics (PTA) is also used to emphasize connection to the nonequilibrium temperature field. Sensitivity of the PTA technique to optical contrast in biological tissues and ability to detect chromophores at depths of several centimeters with millimeter spatial resolution are the two main reasons for the rapid development of this imaging modality in recent years. Conventional use of the PTA method consists of short pulse (nanosecond) optical excitation of a test specimen

and time-resolved detection of acoustic transients received by a broadband ultrasonic transducer or an array of transducers.<sup>5</sup> The spatially resolved images can be obtained either by employing a numerical tomographic reconstruction algorithm or by use of a focused ultrasonic transducer, which can be scanned over the region of interest. Regardless of which reconstruction method is used, the depth information in the time-domain measurements is recovered from the acoustic wave travel times, while the optical absorption coefficient can be derived from the shape of an acoustic profile.<sup>6,7</sup> An alternative approach to PTA imaging is based on periodic optical excitation and frequency-domain signal processing to obtain spatially resolved images of tissue chromophores. Frequency-domain PTA (FD-PTA) was originally proposed and successfully demonstrated in our experiments with tissue phantoms and *ex vivo* tissue samples.<sup>8-10</sup> Subsequent and independent studies<sup>11</sup> confirmed several valuable features of the Frequency Domain PA method. Both time-domain PTA and FD-PTA imaging modalities possess distinct and attractive features that may eventually be adopted commercially. For example, the pulsed PTA response is usually high in amplitude and image

---

Address all correspondence to: Sergey A. Telenkov, Center for Advanced Diffusion-Wave Technologies, Department of Mechanical and Industrial Engineering, University of Toronto, 5 King's College Road, Toronto, ON M5S 3G8, Canada. Tel: 416-978-1287; Fax: 416-978-6160; E-mail: sergeyt@mie.utoronto.ca

reconstruction is fairly straightforward. On the other hand, FD-PTA is characterized by high signal-to-noise ratio (SNR) and depth selectivity can be realized using spectral domain filtering.<sup>9</sup> Ultimately, preference for one technique or another depends on the particular imaging application the PTA method tries to address. Maximum imaging depth and spatial resolution is especially important for noninvasive imaging of breast cancer because the depth of a tumor may exceed several centimeters.<sup>12,13</sup> Therefore, it appears important to have quantitative characterization of various PTA imaging methods with respect to the maximum imaging depth that can be achieved with specific instrumentation. We address this objective in the present work using a dual-mode laser system capable of both pulsed nanosecond and relatively long continuous wave (CW) intensity modulated optical excitation of our test samples under the same experimental conditions. To the best of our knowledge, this is the first experimental study that directly compares time-domain PTA and FD-PTA measurements with respect to depth sensitivity in biological materials.

## 2 PTA Signal Generation

The theory of photothermal generation of acoustic waves in solid and liquid materials was described in several theoretical studies.<sup>5,14,15</sup> The PA response from subsurface chromophores depends on the details of photon propagation in surrounding tissues. The diffusion approximation describing the optical fluence  $E(\mathbf{r}, t)$  as a photon density wave is frequently employed to simplify the complex photon transport phenomenon in biological materials.<sup>16</sup> The diffusive nature of photon flux in tissue results in significant broadening of the initially collimated laser beam, which creates a nearly uniform irradiation pattern for relatively small tissue chromophores. In the case of nanosecond laser irradiation, the time dependence is modeled as a  $\delta$  function and conductive heat transfer is neglected. Assuming that the thermoelastic effect is the dominating mechanism in laser PA energy conversion, the maximum acoustic pressure  $p_0$  at the chromophore surface is estimated as

$$p_0 = c_a^2 \rho \beta \Delta T = \frac{c_a^2 \beta \mu_a E_0}{C_p} = \Gamma \mu_a E_0, \quad (1)$$

where  $\Delta T$  is the optically induced temperature increase,  $\mu_a$  is the absorption coefficient,  $c_a$  is the speed of sound,  $\rho$  is the tissue density,  $\beta$  is the isobaric volume thermal expansion coefficient and  $C_p$  is the specific heat at constant pressure. The Grüneisen coefficient  $\Gamma = c_a^2 \beta / C_p$  combines thermoelastic properties and defines the efficiency of the PA generation. If the size of the heated area is much smaller than the distance  $R$  to the detector, then the initial pressure (1) propagates as a bipolar spherical wave with amplitude decreasing as  $1/R$ . The duration  $t_a$  of the transient acoustic response depends on both the duration of laser exposure and the spatial extent of photothermal sources, which is determined by the material absorption coefficient  $\mu_a$ . In the case of short time laser irradiation,  $t_a$  is equal to the acoustic transit time across the optical penetration length [i.e.  $t_a = (c_a \mu_a)^{-1}$ ]. In our experiments, we are concerned with measurements of the peak acoustic pressure received by an ultrasonic transducer rather than with the detailed profile of the acoustic response. To maximize sensitivity, the test samples were positioned at the focal plane of a

circular focusing transducer with the laser beam aligned to heat the focal zone. Although the scattering media will inevitably expand the laser spot, the size of the transducer focal area remains unchanged and can be considered as a source of spherical acoustic waves emitted into the coupling media. For a spherically symmetric PTA source with radius  $r_s$ , the peak acoustic pressure at the focal distance  $R$  is estimated as

$$p(R) = \frac{1}{2} \frac{p_0 r_s}{R}. \quad (2)$$

The electric signal produced by the transducer is proportional to the total pressure received by a circular aperture with the area  $A_d$

$$p_d = \frac{p_0 r_s}{4 \pi R^3} A_d. \quad (3)$$

In our experiments, the spatial and thermoelastic parameters remained fixed; therefore, any observed changes in acoustic signal were solely due to changes of the initial pressure  $p_0$  caused by the variations of optical fluence  $E$  at various depths inside the scattering medium.

A periodically modulated laser beam stimulates temperature oscillations (thermal waves) in the sample which, in turn, produce harmonic acoustic pressure waves. This type of photogeneration was developed extensively for spectroscopic<sup>17</sup> material characterization using measurements of the PTA amplitude and phase. Our use of FD-PTA differs from the conventional spectroscopic applications mainly because it enables spatially resolved imaging with a modulated laser source. Similar to short-pulse excitation, the thermal diffusion length in tissue at megahertz modulation frequencies is extremely short and the region of optical absorption limits the spatial extent of periodic acoustic sources. Normally, the specific modulation frequency range is chosen in the context of a particular application. The frequency range of 0.5–5 MHz, which corresponds to acoustic wavelengths  $\lambda_a = 0.3$ –3 mm in water (speed of sound  $1.5 \times 10^5$  cm/s) is the most suitable for imaging deep-tissue chromophores. Use of low-frequency signals results in reduced spatial resolution, while acoustic waves with frequencies of  $>5$  MHz suffer from increased acoustic attenuation, which limits the imaging depth. A single frequency spherically symmetric photothermal source positioned at  $r_0$  generates divergent acoustic waves with pressure<sup>18</sup>

$$p(R, t) \sim \frac{p_0(r_0, \omega)}{R} e^{-i\omega(t-R/c_a)}, \quad (4)$$

where the PTA frequency spectrum  $p_0(\mathbf{r}_0, \omega)$  defines the amplitude and phase of acoustic waves at the angular frequency  $\omega$ , and  $R = |\mathbf{r}_d - \mathbf{r}_0|$ . Derivation of the PA spectrum  $p_0(\mathbf{r}_0, \omega)$  can be done from analysis of the wave equation for a harmonic response under specific boundary conditions. Assuming slow heat conduction and ideal acoustic impedance matching with a coupling medium, the PTA spectrum of emitted pressure waves is<sup>5</sup>

$$p_0(r_0, \omega) = \frac{c_a^2 \beta}{2C_p} \cdot \frac{\mu_a E(r_0)}{\mu_a c_a - i\omega}. \quad (5)$$

Equation (5) indicates that efficient PTA generation is limited to the bandwidth  $\mu_a c_a$ . The physical meaning of the characteristic frequency  $\omega_a = \mu_a c_a$  consists of matching the absolute value of the acoustic wave vector  $\omega_a/c_a$  to the optical absorption coefficient  $\mu_a$ . The PTA generation is less efficient at frequencies  $\omega > \mu_a c_a$ , resulting in significant decrease of the acoustic response amplitude. The harmonic pressure signal [Eq. (4)] can be measured with high SNR using narrowband coherent detection (a lock-in amplifier), but it is unsuitable for depth-resolved imaging due to its extremely narrow bandwidth. In order to facilitate depth-selective imaging and take advantage of the superior SNR of coherent signal processing methods, FD-PTA with frequency-swept (chirped) optical excitation was introduced.<sup>8,9</sup> The typical PTA response in this case is a frequency-modulated acoustic wave with amplitude  $p_0(\mathbf{r}_0, \omega)$  dependent on the instantaneous frequency and delayed by the travel time  $\tau = R/c_a$ .

Quantitative comparison of time-domain PTA and FD-PTA modalities is challenging due to the vast difference in the power of optical sources utilized for acoustic wave generation. The obvious way to amplify the PTA response is increase of optical irradiation of tissue. Practical limits to optical exposure are imposed by the international safety standards. For example, the ANSI standard<sup>19</sup> quantifies the maximum permissible exposure (MPE) levels for various modes of laser radiation. The MPE for nanosecond laser exposure of skin at 1064 nm is 100 mJ/cm<sup>2</sup> and for long time exposure ( $t_L = 1 \text{ ms} - 2 \text{ s}$ ), MPE = 0.98–6.5 J/cm<sup>2</sup>. Because we are interested in the maximum imaging depth, it is reasonable to compare time-domain PTA and FD-PTA modalities at optical irradiation near the corresponding MPE levels. In the present experiments, all measurements were conducted with fixed laser output settings (pulsed and CW) to ensure optical irradiation below the MPE. No specific normalization of data was done to show the signal behavior at the defined parameters of laser irradiation. It is straightforward to scale the PTA response to corresponding MPE values because of the linear dependence of the acoustic pressure  $p_0$  on the laser fluence  $E$ .

### 3 System Overview and Measurement Procedure

#### 3.1 Dual-Mode PA System

To conduct the comparative study, we employed a dual-mode laser system (Fig. 1) capable of rapid change between pulsed (nanosecond) and intensity-modulated CW optical excitation modes. A Q-switched laser (Continuum, Santa-Clara, CA) was used to generate pulses of near-IR radiation at 1064 nm and 5 ns duration with the repetition rate of 10 Hz. The laser beam was expanded to 4.5 mm FWHM diameter, and the pulsed radiation with average energy of 1.6 mJ ( $E = 10 \text{ mJ/cm}^2$ ) was incident on the sample at an 18-deg angle. The radiation from the CW laser (IPG Photonics, Boston, Massachusetts), with mean power of 300 mW at the same wavelength (1064 nm) and beam diameter of  $\sim 2 \text{ mm}$ , was used to generate periodic acoustic waves by modulating the continuous intensity output using an acousto-optic modulator

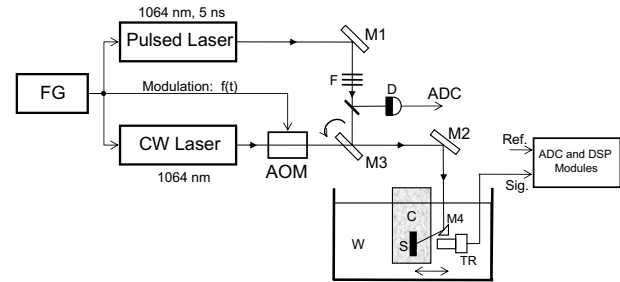
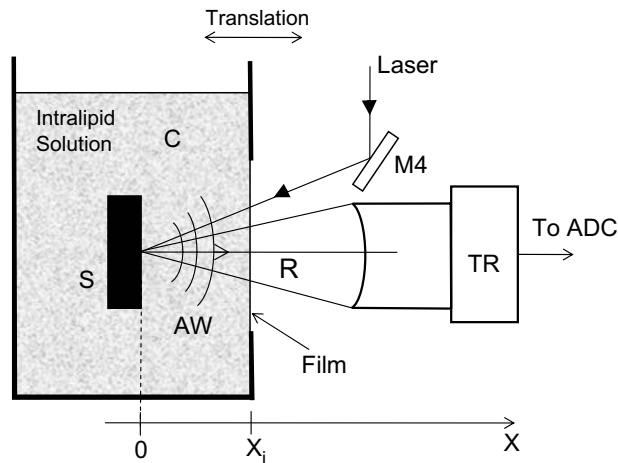


Fig. 1 Dual-mode PTA experimental setup for time-domain and FD measurements. See text for acronyms and labels.

(AOM). The digital modulation (chirp) waveform  $f(t)$  with parameters specific to the experiment was synthesized using LabView software and was uploaded to the NI-5443 (National Instruments, Austin, Texas) modular function generator (FG), which was also used to synchronize the data-acquisition process. The finite length of the modulation waveform constitutes the duration of one signal acquisition event. The typical duration of chirped waveforms was 1 ms with occasional increase to 5 ms for deep chromophore positions. Although a single chirp laser exposure expressed in energy units  $E = 10 - 50 \text{ mJ/cm}^2$  was significantly below the MPE level (978 mJ/cm<sup>2</sup> and 1.46 J/cm<sup>2</sup> for  $t_L = 1 \text{ ms}$  and 5 ms, respectively), the generation of multiple chirps needed for signal averaging may easily attain the MPE limit. The modulation function  $f(t)$  remained the same between consecutive acquisitions, enabling coherent averaging of the individual chirped acoustic signals to increase the SNR. To alternate between pulsed and CW modes, the flipper-mirror (M3) was used to direct one beam or the other through the common path toward the test sample. We simulated the scattering properties of tissue using aqueous solutions of Intralipid suspension with various concentrations to relate the maximum imaging depth to the optical parameters of the surrounding media. Light-absorbing samples made of a stained PVC Plastisol<sup>20</sup> were suspended in a rectangular container (C) filled with the Intralipid solution to simulate tissue chromophores. One wall of the rectangular container was replaced with a thin transparent plastic film window to allow optical radiation to enter the solution and acoustic waves to reach the ultrasonic transducer (TR) unobstructed. The plastic film window also prevented the solution from mixing with clear water in the bath (W) used for acoustic coupling. The Plastisol samples (S) simulating tissue chromophores were stained with black paint to stimulate light absorption. In the reported experiments, we used two samples (samples 1 and 2) with absorption coefficients  $\mu_a = 6$  and  $2 \text{ cm}^{-1}$ , respectively. As shown in Fig. 2, all measurements were done in the backpropagation or reflection mode, which implies that a single surface is used for optical excitation and acoustic detection as opposed to the transmission mode, which requires two-surface access to the test specimens.

#### 3.2 Measurement Procedure

The detailed diagram explaining the relative position of the key elements and the detection principle is shown in Fig. 2. It is important to note that in our experiments the sample (S),



**Fig. 2** Schematic of acoustic wave photogeneration and detection for a test sample immersed in Intralipid solution.

ultrasonic transducer and steering mirror (M4) were stationary, suspended independently on the Intralipid container (C). At the same time, the container C was attached to a micropositioning stage to enable precise translations of the whole container and, therefore, changing the sample depth with respect to the interface film separating Intralipid solution and coupling water. The distance  $R$  between absorbing sample and transducer was set equal to the transducer focal distance. Detection of acoustic waves (AW) was done by two ultrasonic transducers (Panametrics) with the peak of frequency response at 3.5 MHz (model no. V382, bandwidth: 2.6 MHz) and 0.5 MHz (model no. V391, bandwidth: 0.3 MHz), and with focal distances of 25 and 50 mm, respectively. The sample-transducer distance was optimized for the maximum of detection sensitivity and remained fixed during the measurements. The sample depth  $X_i$  was varied from 1 to 25 mm with an increment of 1 mm. The maximum scanning depth of 25 mm was set due to mechanical constraints in the system, specifically because of the focal distance of the high-frequency transducer used in the experiments. The 20% Intralipid stock solution was mixed in clear water at various concentrations from weakly scattering to those similar to breast tissue. Specifically, each of the two absorbing samples (1 and 2) was tested in three solutions of Intralipid<sup>21</sup> with respective concentrations (by volume): 0.12% (solution 1), 0.24% (solution 2), and 0.47% (solution 3). It is expected to observe a rapid decrease of the acoustic signal when depth increases because the number of the initial optical photons that reach the targeted chromophore and are absorbed dramatically decreases. Therefore, the SNR becomes important for imaging of deep subsurface chromophores. The inherent difference in acquisition and processing of broadband acoustic transients (time-domain) and band-limited chirped PTA signals (FD) results in a different SNR. Although the stress-confined pulsed photogeneration is capable of producing high-magnitude acoustic transients, the need for broadband detection also results in high level of noise. The obvious way to increase SNR is the averaging of multiple signal records. In our time-domain measurements, the total  $N=10$  individual signal records were averaged to produce a single acquisition waveform, which requires 1 s for each spatial point at the

repetition rate of 10 Hz. Further increase of  $N$  is possible but appears to be impractical from the standpoint of real-time imaging applications, where rapid signal acquisition and processing of large amounts of data for image reconstruction is essential. Assuming the main source of noise is amplifier thermal noise described by the zero-mean Gaussian probability density function with the standard deviation  $\sigma$ ,  $N$  independent measurements give the SNR improvement factor  $N^{1/2}$ . Such an averaging principle is fundamentally incoherent because each point of the PTA signal is averaged independently. In contrast to the time-domain technique, the FD-PTA method employs coherent signal processing (correlation processing), meaning that the entire signal is integrated to produce a single output datum. This processing technique requires exact knowledge of the phase relationship between the detected signal and the signal used as a reference. Detailed SNR analysis reported in the literature<sup>22</sup> demonstrates additional improvement in SNR when multiple waveforms are added coherently at the preprocessing stage to multiply the energy of the individual chirps. In our experiments, duration of the modulation waveform  $f(t)$  was set to 1 or 5 ms, which means that a much larger number of individual signals can be recorded and averaged coherently over the same time period of 1 s. However, there are practical limitations in this case as well, mainly related to storage and rapid transfer of large amounts of data comprising the long-duration waveforms acquired with high sampling rate. In our FD measurements,  $N$  was varied between 100 and 400 to improve the SNR of weak signals. The measurement procedure common to both modes consisted of the following steps: (i) container C with specific concentration of Intralipid was brought to the starting position ( $X=0$  mm); (ii) the test sample was placed inside the container in direct contact with the interface film; (iii) the PTA signal was obtained and the transducer distance was optimized; (iv) the container was translated with step  $\Delta X=1$  mm up to  $X=25$  mm, and the averaged signals were recorded at each position. The recorded averaged data were combined in a 2-D matrix and transferred to an appropriate signal-processing unit for further analysis.

### 3.3 Data Processing and Analysis

Specifics of data processing differ for signals acquired in the two operating modes. The main concern for time-domain PTA is a reliable measurement of the profile and delay times of the acoustic transients received by a wideband transducer. The SNR is very important for imaging of deep chromophores; therefore, the high repetition rate of laser pulses is essential for averaging multiple signals recorded at different spatial positions. Typically, hundreds of individual signals must be averaged to achieve substantial noise reduction, which significantly increases the time needed for data acquisition and image reconstruction. In contrast to the relatively straightforward time-domain measurements of a delayed PTA peak, the acoustic signals with frequency-swept response require a more sophisticated signal-processing algorithm to recover spatially resolved information. We used two signal-processing methods in the present study to compare to the time-domain data. The first algorithm computes the cross-correlation function of a recorded PTA response and a stored replica of the modulation waveform (correlation processing). The second

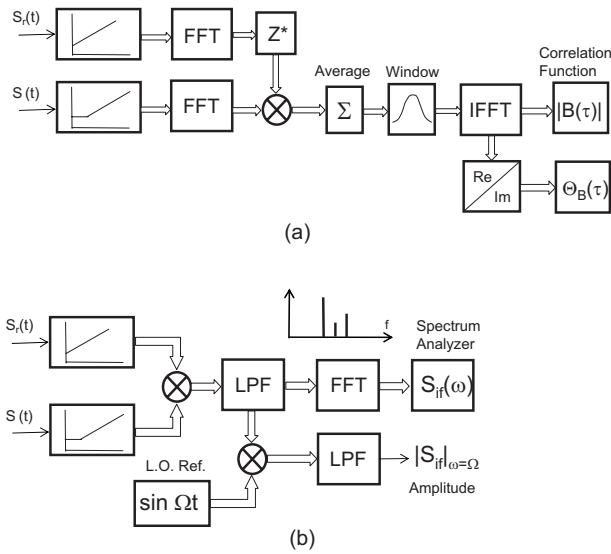


**Fig. 3** Two signal processing algorithms for the linear frequency-swept acoustic signals: (a) Correlation processing and (b) spectrum analyzer processing.

utilizes heterodyne mixing and computes the spectrum of an intermediate signal obtained by frequency downshifting (spectrum analyzer processing). Both algorithms were originally developed for radar and sonar applications and are described extensively in the literature.<sup>23</sup> It was mentioned above that narrowband signals [Eq. (4)] cannot be used for depth-resolved imaging. Following the theory of radar signals, the requirement of high SNR and high spatial resolution can be met if the modulation waveform is frequency modulated to expand its bandwidth. The simplest form of frequency modulation is a linear frequency sweep, which is merely a sinusoidal wave with the quadratic phase dependence

$$\theta(t) = \omega_1 t + b \frac{t^2}{2}, \quad (6)$$

where  $\omega_1$  is the chirp-starting frequency and  $b$  is the sweep rate. Because temperature oscillations follow the laser-heating pattern, it is expected that the PTA response will be linear frequency modulated (LFM) as well, with the instantaneous amplitude dependent on frequency. Detection of the LFM acoustic waves can be done by the same transducer provided its frequency response is consistent with the chirp bandwidth. The depth information is recovered at the signal processing stage assuming the speed of sound remains constant. The first method of LFM signal processing is based on matched filtering and is shown in Fig. 3(a). Using Fourier transforms, the output  $s_{\text{out}}(t)$  of a filter is expressed in standard form

$$s_{\text{out}}(t) = \frac{1}{2\pi} \int_{-\infty}^{\infty} H(\omega) S(\omega) e^{i\omega t} d\omega, \quad (7)$$

where  $H(\omega)$  is the filter spectral response and  $S(\omega)$  is the spectrum of the input signal  $s(t)$ . It is simple to demonstrate<sup>24</sup> that the output SNR is maximized for a signal masked by white noise, if the filter spectral response is the complex conjugate of the input signal spectrum [i.e.,  $H(\omega) = A \cdot S^*(\omega)$ ,

where  $A = \text{const}$ ]. Mathematically, matched filtering represents the time correlation processing of a noisy signal  $s(t)$ , with an exact replica of the signal known *a priori*. Then, the output of the matched filter [Eq. (6)] is equivalent to the autocorrelation function

$$B(t) = \int_{-\infty}^{\infty} s(t' + t) s(t') dt' = \frac{1}{2\pi} \int_{-\infty}^{\infty} |S(\omega)|^2 e^{i\omega t} d\omega. \quad (8)$$

Typically, a copy of the modulation waveform is stored and used as a reference to compute the correlation function with the received signal. The result of correlation processing of a signal delayed by  $\tau$  is a sharp peak at time  $t = \tau$ , indicating the presence of a signal coherent with the reference. The magnitude of the peak is equal to the signal energy  $E_s$ , and SNR for thermal noise with uniform power spectral density  $N_0/2$  is  $2E_s/N_0$ . It is worth noting that correlation processing does not provide detailed information about the waveform but rather indicates the presence or absence of a waveform with specific characteristics. In practice, the received signal may not be an exact copy of the reference and signal phase may not be known in advance. Then, Eq. (8) gives a cross-correlation function and the SNR gain may be less than the optimal provided by the ideal matched filter. Additionally, the spectrum of the PTA signal is reduced at the high-frequency end [Eq. (5)], which also translates into reduced signal energy and SNR smaller than ideal.

Implementation of correlation processing is much more efficient in the Fourier domain [Fig. 3(a)], and the resulting complex valued correlation function  $B$  can be analyzed in terms of amplitude  $|B|$  and phase  $\theta_B = \tan^{-1}(\text{Im}B/\text{Re}B)$ . It is important to note that the correlation phase  $\theta_B$  defined in this manner is different from the acoustic wave phase. It describes the fine structure of the correlation function  $B$ , which gives it the connection to the physical properties of the probed domain and is completely determined by the chirp parameters. In the case of LFM chirps with duration  $t_{\text{ch}}$  and quadratic phase dependence [Eq. (6)], the correlation function  $B(t)$  has a sinc-function envelope filled with a harmonic carrier at the frequency  $\omega_0 = \omega_1 + (bt_{\text{ch}})/2$ , which is equivalent to the linear phase  $\theta_B = \omega_0 t$  as a function of time. The phase  $\theta_B$  of the correlation function can be utilized for imaging as well, but meaningful phase dependence can be obtained only near the correlation peaks where  $\text{SNR} > 1$ . The advantage of phase is related to its insensitivity to local variations of optical fluence, which may be used to produce more uniform depth-specific images than those obtained with amplitude data alone.<sup>9</sup> Phase detection of the acoustic wave itself requires separate in-phase and quadrature processing channels and was not implemented in the present studies. Regardless of the specifics of phase processing, it is important to note that the phase data can be used in PTA imaging to yield information complementary to amplitude, whereas pulsed laser PTA imaging is capable of yielding only one such image (magnitude).

The second method is called the “spectrum analyzer” technique, which is based on heterodyne mixing to extract depth information from the received PTA response. The block diagram of the algorithm is shown in Fig. 3(b). This algorithm multiplies the input signal  $s(t)$  delayed by time  $\tau = R/c_a$ , and the reference chirp  $s_1(t)$  with phase characteristic given by Eq.

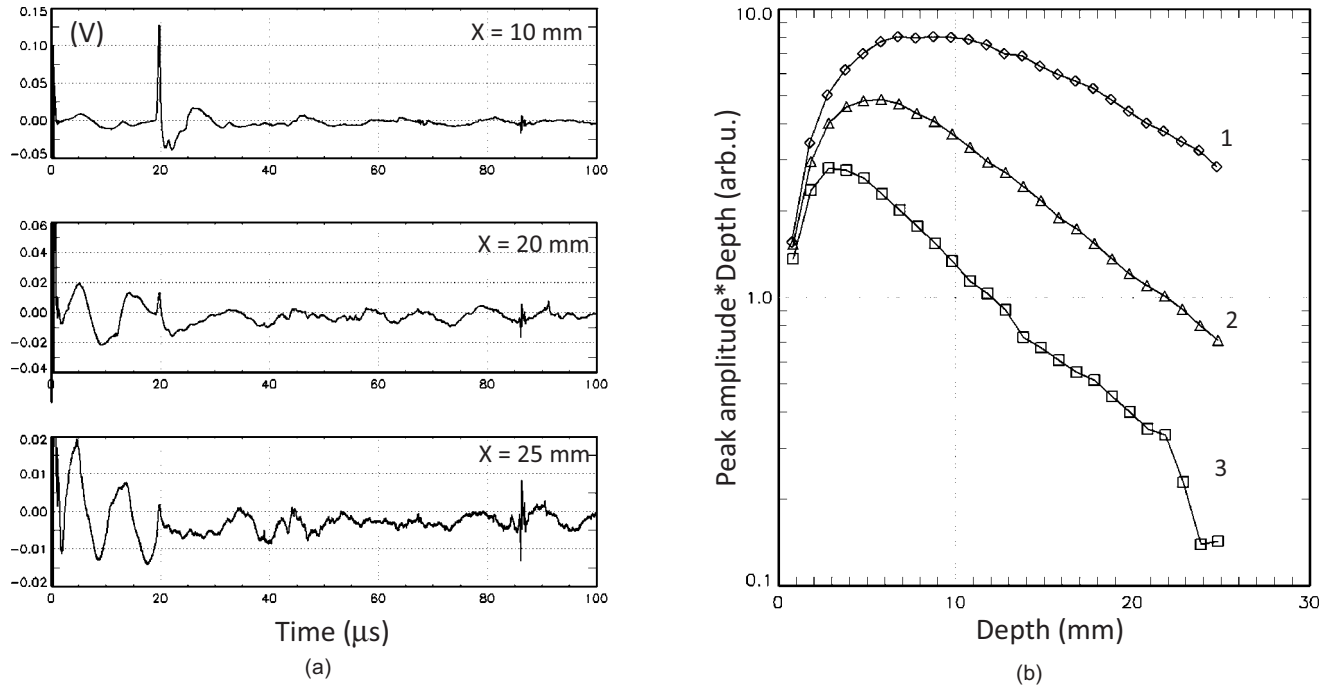


**Fig. 4** Time-domain signal (a) for sample 1 in the high-scattering Intralipid solution (0.47%) at three depth positions  $X=10, 20,$  and  $25$  mm recorded with a high-frequency (3.5 MHz) transducer; (b) product of the signal amplitude and the sample depth versus depth for the three Intralipid solutions (1–0.12, 2–0.24, and 3–0.47%).

(6). The multiplication and subsequent rejection of the sum components in a low-pass filter results in an intermediate frequency signal  $s_{if}(t)$  in the form

$$s_{if}(t) = \langle s_r(t)s(t - R/c_a) \rangle = \frac{1}{2}A \cos\left(b\frac{R}{c_a}t + \theta\right), \quad (9)$$

where  $A$  is the signal amplitude and  $\theta$  is the constant phase. Equation (9) shows that the new signal  $s_{if}(t)$  should have the frequency component  $\omega_{if}=bR/c_a$  proportional to the delay time  $\tau=R/c_a$ . This fact allows one to recover depth information from analysis of the spectrum of  $s_{if}(t)$ . Thus, the spectrum analyzer algorithm enables direct mapping of the delay times of the received PTA response into the frequency spectrum of the intermediate signal, which can be examined with high precision, for instance, using a lock-in amplifier.

## 4 Results and Discussion

### 4.1 Time-Domain Results

Results of the time-domain measurements are summarized in Figs. 4 and 5. The PTA response from the test samples was obtained in all Intralipid solutions and had similar bipolar profiles with magnitude scaled according to the sample absorption coefficient. Typical signals recorded with the 3.5-MHz transducer and sample 1 positioned at the depths  $X=10, 20,$  and  $25$  mm in solution 3 are shown in Fig. 4(a). Because sample position with respect to the transducer did not change, the peak of the PA signal was always observed at 20- $\mu$ s delay time regardless of the position of the water-solution interface. The amplitude of the positive peak was measured as a function of the sample depth and the Intralipid concentration. Two characteristic features are apparent from

the traces in Fig. 4(a) (i) the PA signal rapidly decreases with depth increase, and (ii) the signal becomes progressively obstructed by the interference signal observed at  $t < 20 \mu$ s. That interference signal originates in the scattered optical radiation absorbed by the transducer itself and the resulting sound waves reflected from the transducer housing. Frequently, additional signal conditioning is employed to reduce the effect of interference (e.g., digital filtering), but we do not use it here to avoid possible alterations to the broadband PTA signal itself. Measurements of the signal amplitude as a function of depth for all three Intralipid solutions and the two absorbing samples are shown in Figs. 4(b) and 5. The gradual decrease of the PTA amplitude with increasing sample depth can be used to evaluate optical properties of the surrounding medium. Because the peak of the acoustic pressure is proportional to the local optical fluence  $E$ , the spatial distribution of  $E$  in the diffusion-dominated regime is described in a manner similar to the amplitude of spherical waves

$$E(r) \sim E_0 \frac{e^{-\mu_{eff}r}}{r}, \quad (10)$$

where  $E_0$  is the optical fluence at the interface and  $\mu_{eff}$  is the effective attenuation coefficient. Then, the product  $p_d r$  is proportional to  $\exp(-\mu_{eff}r)$ . A semilog plot of the PTA signal amplitude multiplied by the sample depth versus depth for all three Intralipid solutions is shown in Fig. 4(b). The transition from the collimated laser beam to the diffuse propagation is observed as eventual emergence of a linear trend in the plot, which occurs earlier in the case of the highly scattering solution 3. Thus, the  $\mu_{eff}$  can be estimated from the negative slope of the linear portion of the corresponding curves. The data in

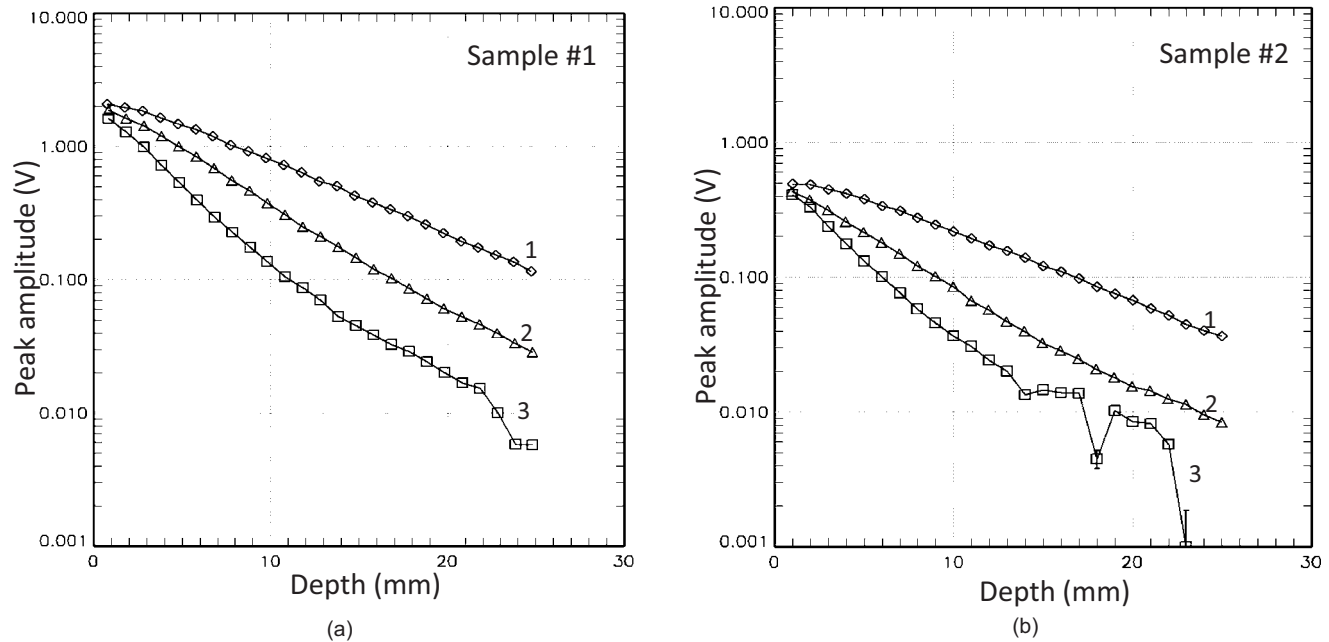


Fig. 5 Amplitude of the acoustic transients as a function of depth for three concentrations of the Intralipid solution (1–0.12, 2–0.24, and 3–0.47%) and two absorption coefficients: (a) 6 and (b) 2  $\text{cm}^{-1}$  of the subsurface inclusions.

Fig. 4(b) give the following estimates for the  $\mu_{\text{eff}}$ : 0.8  $\text{cm}^{-1}$  (solution 1), 1.0  $\text{cm}^{-1}$  (solution 2), and 1.3  $\text{cm}^{-1}$  (solution 3). With respect to maximum imaging depth in tissue, of particular interest are the data recorded with the highly scattering solution (solution 3), which resembles the optical properties of a human breast. Measurements of the signal amplitude as a function of depth for two test samples are shown in Fig. 5. These semilog plots show a nearly linear drop of the acoustic amplitude for the weakly scattering medium that increasingly deviates from the linear with increase of Intralipid concentration. Both samples can be reliably detected in weakly and intermediately scattering solutions (1 and 2). However, in solution 3, the PA signal disappears at a depth of  $\sim 23$  mm (sample 1) and  $\sim 18$  mm (sample 2). Error bars in Fig. 5(a) do not exceed the size of the symbols. Although, the thermal noise in these measurements is relatively small ( $V_{\text{rms}}=5 \times 10^{-4}$  V), the background interference shown in Fig. 4 becomes the dominant blocking factor, which cannot be reduced by simple averaging of multiple waveforms. It should be noted that theoretical estimates of maximum imaging depth frequently rely exclusively on the thermal noise level as a limiting parameter.<sup>2,12</sup> Although such estimates may be appropriate for the transmission imaging mode where optical source and transducer are positioned at opposite sides, single-side reflection imaging must deal with interference stemming from the direct optical radiation and background absorption of the surrounding tissues. Assuming idealized interference-free measurements, we can estimate the maximum depth by extrapolating curves in Fig. 5 to the thermal noise floor. Our measurements give for samples 1 and 2 the potential maximum imaging depth of about 45 and 35 mm, respectively, for the given sensitivity of the ultrasonic transducer and thermal noise-limited detection. In practice, these estimates are reduced nearly by a factor of 2 unless additional measures (e.g.,

dark-field illumination<sup>25</sup>) are implemented to eliminate photoacoustic interference.

Similar time-domain measurements were carried out with the 2-in. focusing ultrasonic transducer with the central frequency of 0.5 MHz, and results are shown in Fig. 6. Typical waveforms at depths of  $X=10$ , 20, and 25 mm are shown in Fig. 6(a), and the amplitude dependence of the PTA signals for the same two samples in solution 3 is shown in Fig. 6(b). Because focal distance is increased by the factor of 2, the PTA response is detected at 40- $\mu\text{s}$  delay time. Our data indicate that the signal can be detected as deep as 25 mm in solution 3, but it appears on top of a low-frequency background interference pattern resulting in increased instability of the signal at large depths. Comparing to data in Figs. 4 and 5, the signal amplitude is smaller due to the difference in transducer sensitivity, but the thermal noise appears to be diminished as well, as the result of reduced detection bandwidth. Again, simple extrapolation of the trend to the noise floor ( $1.5 \times 10^{-4}$  V) gives an estimate of the maximum depth, which for both samples is  $<40$  mm. The time-domain data show that broadband detection with 3.5 MHz is preferred and gives the maximum imaging depth of 18–23 mm for the sample absorption coefficient range of 2–6  $\text{cm}^{-1}$ . Potentially, the maximum depth can be extended to 35–45 mm provided efficient signal conditioning is implemented to suppress the background interference signal.

#### 4.2 FD Results with Correlation Processing

It was demonstrated in our earlier studies<sup>8–10</sup> that PTA imaging of tissues with submillimeter depth resolution can be realized with relatively low-intensity modulated laser irradiation, provided the modulation waveform has specific temporal characteristics. Then, the depth information can be recovered

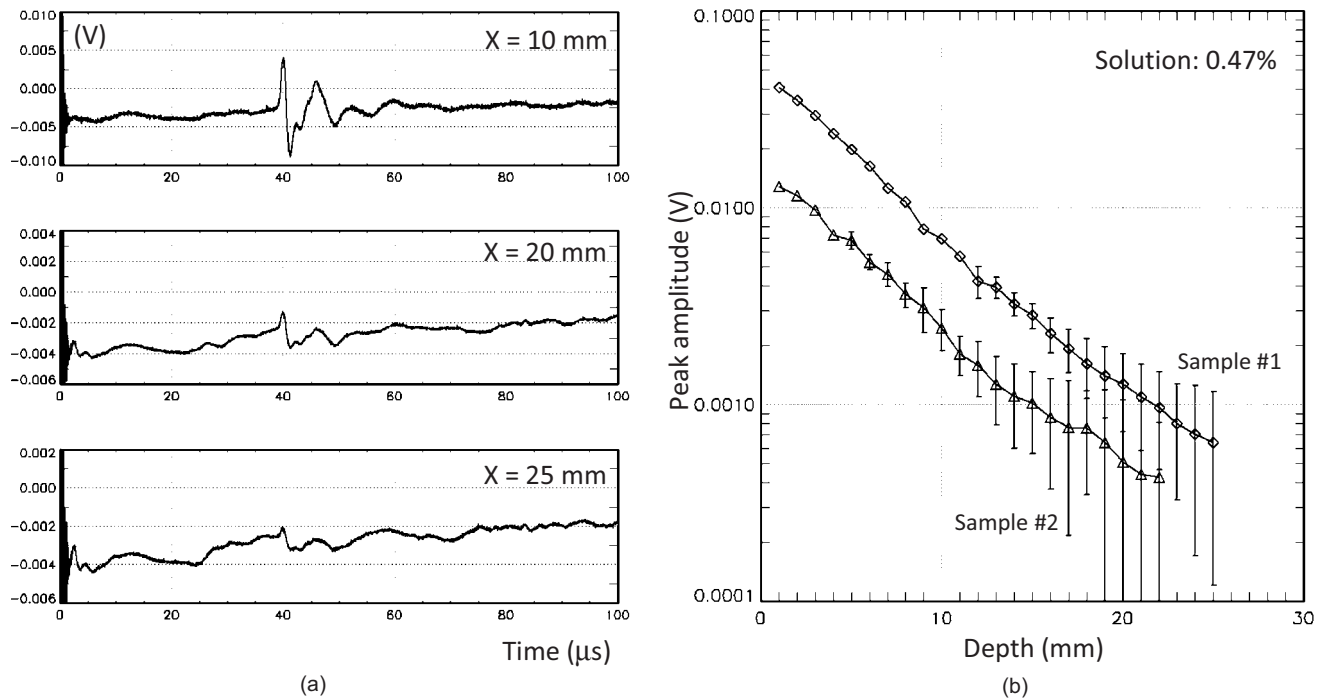


Fig. 6 Time-domain signal and amplitude as a function of depth in Intralipid solution 3 measurements with a low-frequency (0.5-MHz) transducer.

using FD signal processing methods applied to the recorded periodic PTA response. The FD-PTA method utilizes coherent properties of photogenerated acoustic waves as discussed in Sec. 3.3 to increase the SNR of the relatively weak acoustic response. Compared to the time-domain measurements, the FD-PTA gives much greater flexibility in shaping the PTA response (chirp length, frequency range, and sweep rate). Along with coherent signal processing algorithms for signal recovery, it may provide a valuable alternative to the conventional pulsed time-domain technique. To address the question of maximum imaging depth attainable with FD-PTA, we use the same absorbing samples and the same scattering solutions to detect the PTA signal at various depths. The optical excitation in this mode is modulated by a continuous sequence of chirps with the frequency swept in a predefined range. The initial phase of each chirp was maintained fixed to enable coherent averaging of multiple signals prior to signal processing. The correlation processing method shown in Fig. 3(a) computes the amplitude of the cross-correlation function as a function of delay time using an fast Fourier transform (FFT) algorithm. The chirp parameters were varied depending on the transducer spectral response and the sample depth in order to increase SNR. Typically, the linear frequency-swept modulation waveforms were 1 or 5 ms long and in the frequency-sweep range of 1–5 MHz for the high-frequency transducer detection and 200–800 kHz for the low-frequency transducer. Recorded PTA signals were averaged coherently ( $N = 100$ –400), and the averaged signal was cross-correlated with the reference waveform. Typical results of correlation processing for linear-frequency modulated response (chirp duration, 1 ms) recorded with the 3.5-MHz transducer and sample 1 in the high-scattering solution (solution 3) are shown in Fig. 7. The spike at  $t = 20 \mu\text{s}$  corresponds to the PTA response from the sample and is 575 ns wide (FWHM).

Its magnitude decreased rapidly with increase of the sample depth. The plots of the cross-correlation function amplitude versus depth for both samples and all Intralipid solutions are shown in Fig. 8. Similar to the time-domain measurements, the semi-log plot of amplitudes show that the peak of the cross-correlation signal decreases almost linearly and only for solution 1 is a PTA signal observed within the entire range of

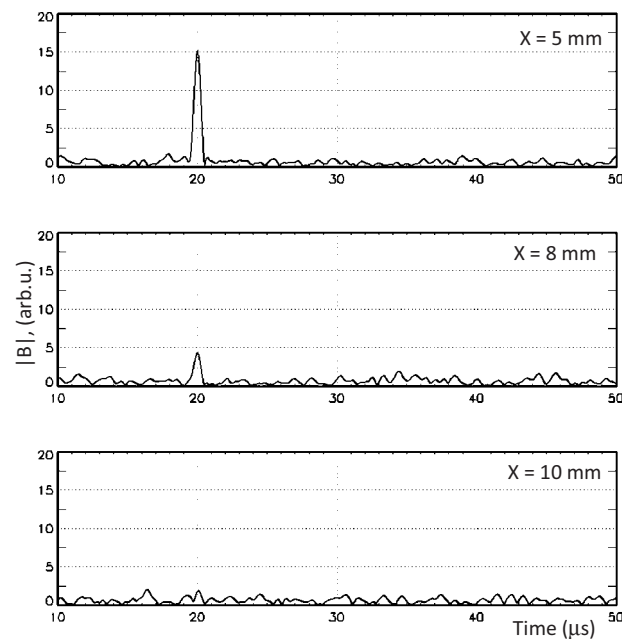
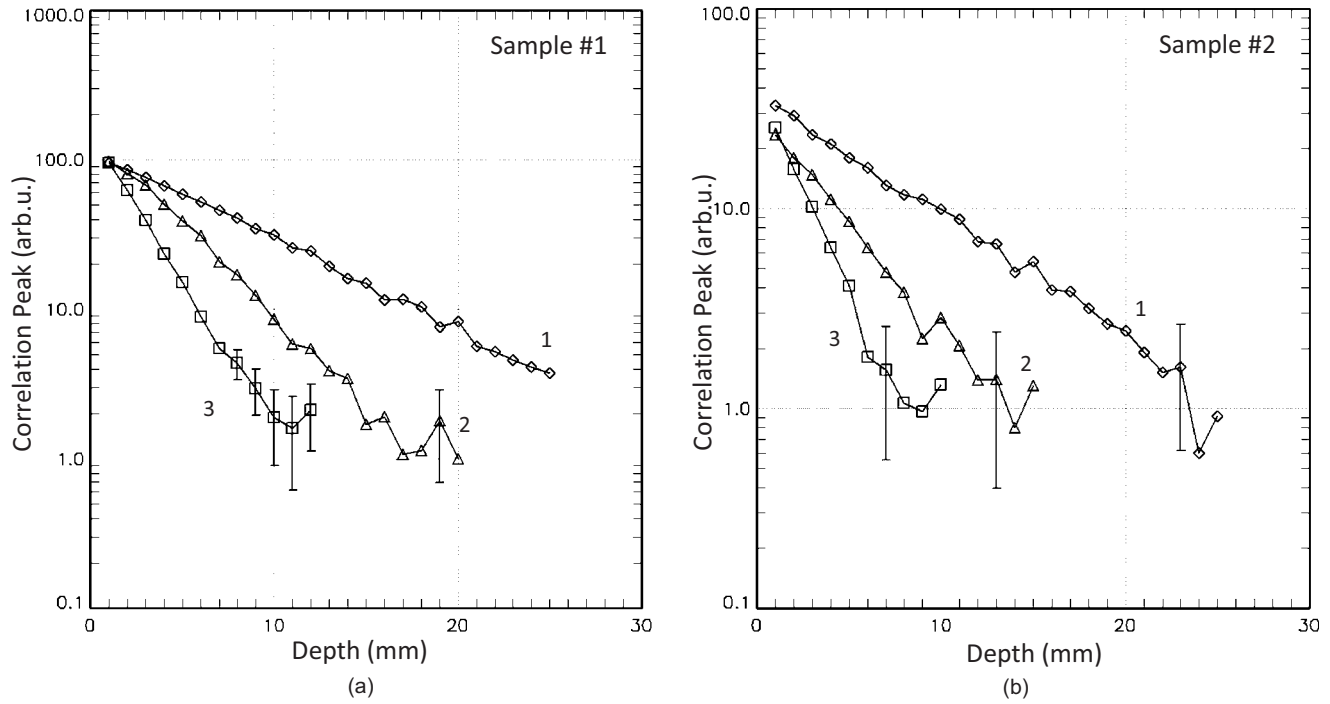


Fig. 7 Cross-correlation function for sample 1 and chirped optical excitation. Chirp parameters: sweep range, 1–5 MHz; duration, 1 ms. Transducer 3.5 MHz.



**Fig. 8** Magnitude of the cross-correlation peak as a function of depth for samples 1 and 2 and three concentrations of the Intralipid solution (1–0.12, 2–0.24, and 3–0.47%). Chirp parameters: sweep range 1–5 MHz, duration 1 ms. Transducer 3.5 MHz.

depths. For the high-scattering solutions, the maximum depth at which the peak remained above the noise floor was ~10 mm for sample 1 and ~8 mm for sample 2. Comparison to Fig. 5 reveals that maximum imaging depths observed

in the time-domain measurements exceed those achieved with chirped excitation nearly by a factor of 2. Despite the inferior results shown in Fig. 8, the performance of the FD method can be significantly improved by varying parameters of the

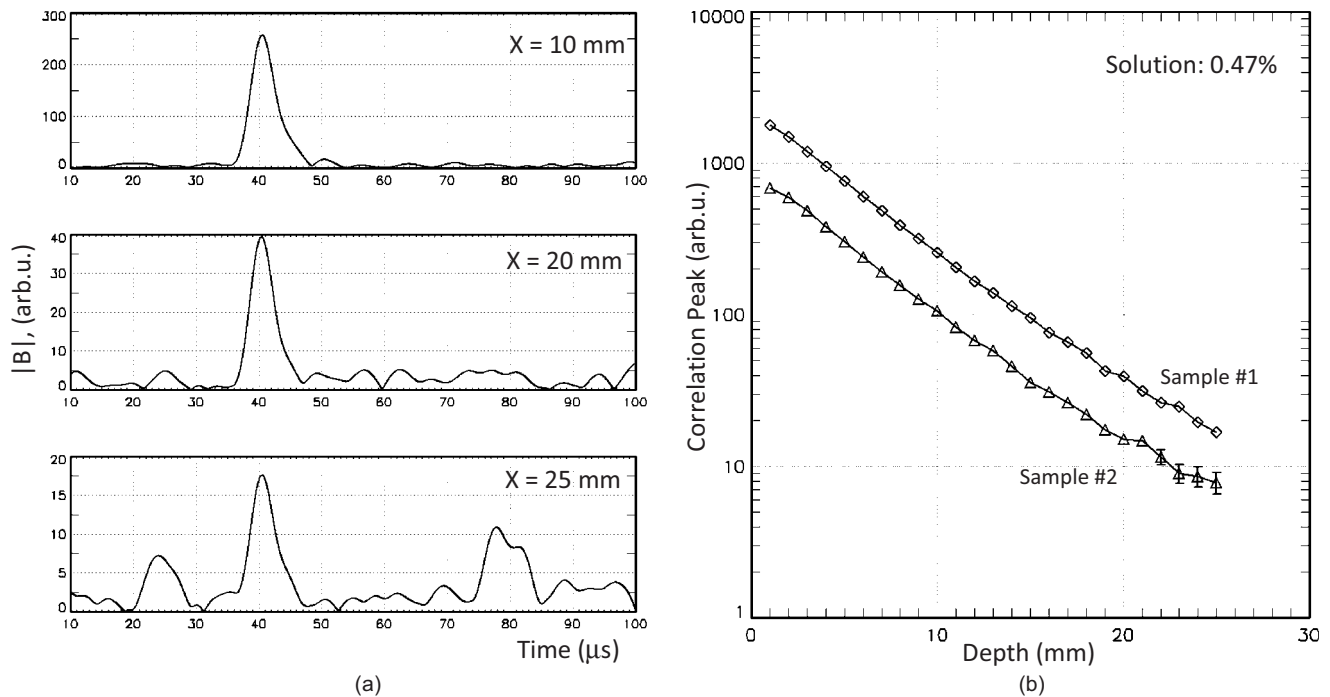


**Fig. 9** (a) Cross-correlation function for sample 1 and chirped optical excitation. Chirp parameters: sweep range 200–800 kHz, duration 5 ms. (b) Magnitude of the cross-correlation peak as a function of depth for samples 1 and 2 in highly scattering Intralipid solution (0.47%). Transducer 0.5 MHz.

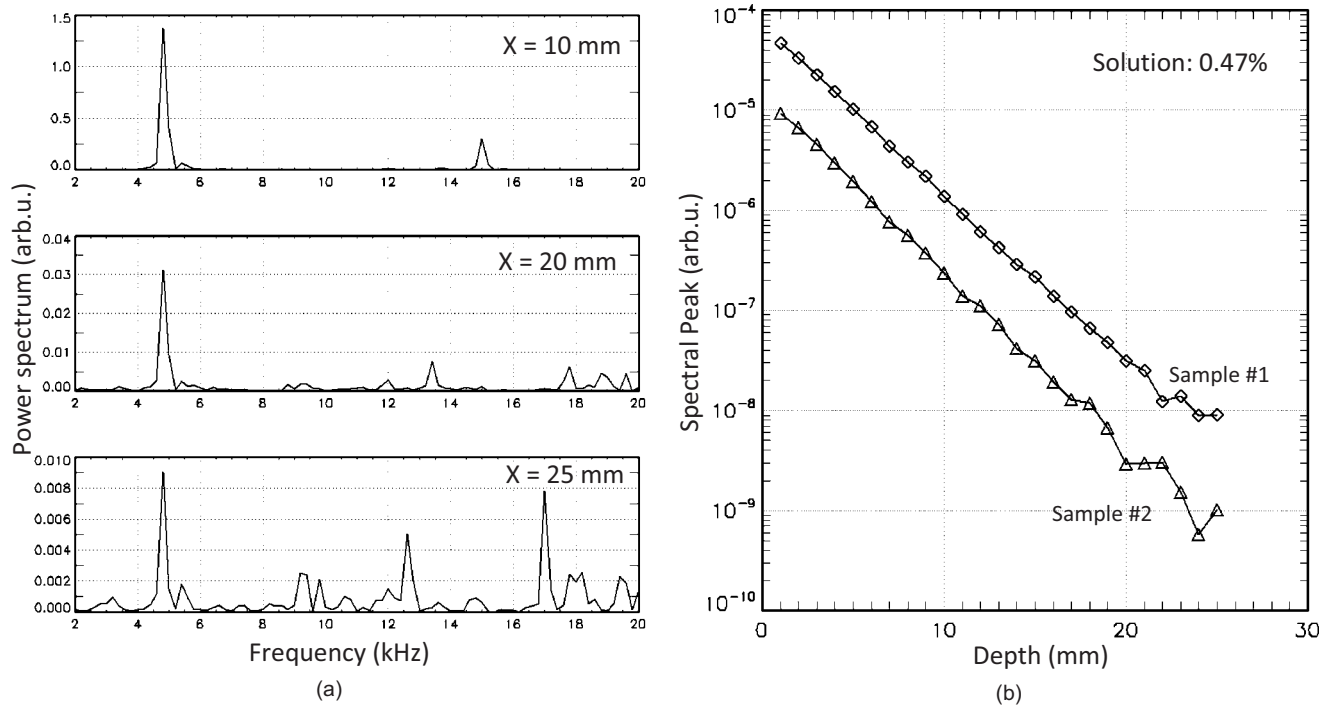


**Fig. 10** Results of spectrum analyzer processing: (a) Power spectrum of the intermediate signal and (b) amplitude of the spectral peak at 4.8 kHz as a function of depth for samples 1 and 2 and Intralipid solution 0.47%.

modulation chirp. There are two parameters to consider: one is the chirp duration; the other is the frequency sweep range. The former parameter defines the SNR because the peak magnitude is proportional to signal energy, and the latter is related to the efficiency of PTA response generation. Measurements with lower frequencies and longer chirps show that the imaging depth of the FD-PTA method can be extended (Fig. 9). A series of measurements with Intralipid solution 3 and the laser modulation chirp in the frequency sweep range of 200–800 kHz (chirp duration 5 ms) were carried out with the low-frequency transducer (0.5 MHz). Results of cross-correlation processing for sample 1 positioned at depths  $X = 10, 20,$  and  $25$  mm are shown in Fig. 9(a). Because the axial resolution is inversely proportional to bandwidth, the correlation peak appears noticeably broader compared to the high-frequency measurements, which ultimately translates into reduced axial resolution. However, in contrast to Figs. 7 and 8, the correlation signal in Fig. 9(a) shows that it is possible to detect PTA signals at a depth of  $>25$  mm. Measurements of correlation peak amplitudes for samples 1 and 2 in solution 3 are shown in Fig. 9(b). Data for other solution concentrations are not shown because the PTA signal was reliably detected for all depths (0–25 mm). Extrapolation of these two measurements to the noise floor gives the potential maximum imaging depth of 32–38 mm for chromophores with the absorption coefficients in the range of  $2\text{--}6\text{ cm}^{-1}$ . These data show that the maximum imaging depth of frequency-domain PTA is comparable to that achieved in the pulsed time-domain measurements (Fig. 5), although an increase in imaging depth requires certain trade-off with respect to the axial resolution. The observed increase in depth sensitivity with low-frequency chirps may be explained by the more efficient PA generation

because the acoustic wavelength  $\lambda_a$  in the range of 200–800 kHz ( $\lambda_a = 1.8\text{--}7.5$  mm) more closely matches the optical penetration depth equal to  $\mu_a^{-1}$ . It is also important to note that FD-PTA with correlation processing is much less susceptible to the unwanted baseline interference (compare Figs. 7 and 9 to Fig. 4) and exhibits a much improved SNR [see Figs. 6(b) and 9(b)] which ultimately may result in a better contrast of photoacoustic images.

#### 4.3 FD Results with Heterodyne Processing

An alternative processing method of the linear-frequency modulated signals was described in Sec. 3.3 and is shown schematically in Fig. 3(b). This algorithm relies on heterodyne-type frequency downshifting, and the intermediate spectrum is analyzed to recover spatial information. The result of multiplication of the reference chirp and the chirped PTA response delayed by the time  $R/c_a$  with subsequent rejection of the sum frequency components (low-pass filtering) creates an intermediate signal  $s_{if}$  with the frequency component  $f_{if} = bR/(2\pi c_a)$  proportional to the delay time. Analysis of the signal  $s_{if}$  spectrum reveals the position of acoustic sources as discrete peaks at frequencies  $f_{if}$ . This algorithm can be very fast because it requires only multiplication operations and forward Fourier transformations, but additional time may be necessary to extract a weak signal from the noisy background. We processed the same data shown in Fig. 9 using the spectral analyzer algorithm to demonstrate its capability with respect to imaging depth. The data recorded with the low-frequency transducer had bandwidth of 600 kHz and chirps were 5 ms long, giving the sweep rate  $b/2\pi = 1.2 \times 10^8$  Hz/s. For the delay time of  $40\ \mu\text{s}$ , the intermediate signal should have a

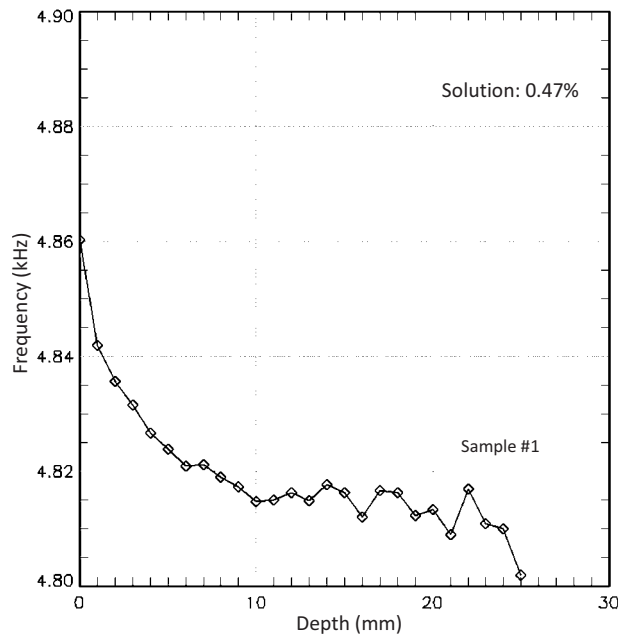


**Fig. 11** Position of the 4.8-kHz peak in the spectrum of the heterodyned signal [see Fig. 10(a)] as a function of depth for sample 1 in Intralipid solution 3 (0.47%).

spectral component at  $f_{if}=4.8$  kHz. The power spectrum of the intermediate signal is shown in Fig. 10(a) for sample 1 at the same depth positions in solution 3 as before. The main peak is observed at 4.8 kHz, as expected, and the secondary peak is due to sound reflection from the interface film. The signal was reliably detected even for the deepest sample position  $X=25$  mm. The relatively narrow width (250 Hz) may compensate to some degree for the loss of axial resolution observed in Fig. 9. Similar measurements of the peak amplitude as a function of depth show the familiar nearly straight line on the semi-log scale with an ultimate depth sensitivity of 25–31 mm (extrapolated data for sample 1), depending on the absorption coefficient. The superior signal-to-noise ratio over the pulsed laser PTA response shown in Fig. 4 is evident. The sharp frequency peak in the spectrum of  $s_{if}$  enables precise measurements of its position as a function of depth. An example of such measurements is shown in Fig. 11. A small but persistent decrease of the peak frequency was observed when the sample depth increased. Because the sample-transducer distance did not change in the course of the depth scan, it is possible to explain the observed phenomenon by a small difference in acoustic wave speed in the Intralipid suspension and in clear water when the relative acoustic travel distance in one medium with respect to the other is changed. Assuming this is the case, the overall shift of 50 Hz translates into sound speed variation of  $\sim 1\%$ . Comparison of the data in Figs. 4–6 and 9–11 underscores the information-rich features, very efficient baseline suppression and superior SNR leading to the high potential of FD-PTA for quantitative characterization of biological materials. Figures 4, 5, and 10 show that FD-PTA with heterodyne processing yields imaging depths comparable to those accessed by pulsed laser PTA, although with somewhat reduced axial resolution.

## Conclusions

We have conducted quantitative characterization of time-domain and FD-PTA measurements with respect to maximum depth sensitivity in materials with optical properties mimicking biological tissues. Experiments were performed using a dual-mode optical system capable of both pulsed laser-induced time-domain and CW FD measurements under identical test conditions. Our results with the nanosecond optical source indicate that the light-absorbing samples in the absorption coefficient range of  $2\text{--}6\text{ cm}^{-1}$  immersed in tissuelike scattering Intralipid suspensions can be detected at maximum depth of 18–23 mm below the surface. The masking effect of the undesired background interference signal is substantial for the pulsed PTA technique at large imaging depths in reflection mode and must be addressed in order to achieve the ideal thermal-noise-limited detection. Estimates of the maximum depth show imaging feasibility at 35–45 mm. Significant increase of imaging depth by increasing optical fluence to the MPE level does not seem possible unless acoustic interference is eliminated without affecting the PTA response. It was also demonstrated that the FD-PTA modality operating with chirped modulation waveforms and much lower optical power can provide comparable or better depth sensitivity with millimeter-scale axial resolution due to superior SNR. Further improvement of the SNR is possible by adjusting the phase of the reference signal to maintain the important in-phase condition and by amplifying the higher-frequency end of a chirp to achieve better matching for correlation processing. In addition to superior SNR, the FD-PTA also provides efficient suppression of the baseline interference, which is important for single surface (reflection) imaging mode. To maximize imaging depth of the FD-PTA technique, the frequency sweep range of the modulation waveforms must be chosen by taking into account the optical properties of the targeted chromophores, which may result in reduced axial resolution. Application of the FD signal processing methods, such as heterodyne mixing, enables direct mapping of spatial information to the spectrum of the frequency-downshifted intermediate signal, which can be used for depth-selective imaging through narrowband filtering. This feature of FD-PTA can be used for the implementation of confocal imaging of biological tissues at substantially improved SNR over pulsed laser PA.

## Acknowledgments

The support of the Ontario Ministry of Research and Innovation through the 2007 Discovery Award in Science and Engineering to A. Mandelis, of the Ontario Research Fund and the Canada Foundation for Innovation for a New Infrastructure Fund, and of the National Sciences and Engineering Research Council for a Discovery Award are gratefully acknowledged.

## References

1. M. Xu and L. Wang, "Photoacoustic imaging in biomedicine," *Rev. Sci. Instrum.* **77**, 041101 (2006).
2. A. Oraevsky and A. Karabutov, "Ultimate sensitivity of time-resolved opto-acoustic detection," *Proc. SPIE* **3916**, 228–239 (2000).
3. A. Gibson, J. Hebden, and S. Arridge, "Recent advances in diffuse optical imaging," *Phys. Med. Biol.* **50**, R1–R43 (2005).
4. D. Huang, E. A. Swanson, C. P. Lin, J. S. Schuman, W. G. Stinson, W. Chang, M. R. Hee, T. Flotte, K. Gregory, C. A. Puliafito, and J. G. Fujimoto, *Science* **254**, 1178–1181 (1991).

5. V. E. Gusev and A. A. Karabutov, *Laser Optoacoustics*, AIP, Melville, NY (1993).
6. A. Karabutov, N. Podymova, and V. Letokhov, "Time-resolved laser optoacoustic tomography of inhomogeneous media," *Appl. Phys. B* **63**, 545–563 (1996).
7. A. Oraevsky, S. Jacques, and F. Tittel, "Measurement of tissue optical properties by time-resolved detection of laser-induced transient stress," *Appl. Opt.* **36**, 402–415 (1997).
8. Y. Fan, A. Mandelis, G. Spirou, and I. A. Vitkin, "Development of a laser photothermoacoustic frequency-swept system for subsurface imaging: theory and experiment," *J. Acoust. Soc. Am.* **116**, 3523–3533 (2004).
9. S. Telenkov and A. Mandelis, "Fourier-domain biphotoacoustic subsurface depth selective amplitude and phase imaging of turbid phantoms and biological tissue," *J. Biomed. Opt.* **11**, 044006 (2006).
10. S. Telenkov and A. Mandelis, "Frequency-domain photothermoacoustics: alternative imaging modality of biological tissues," *J. Appl. Phys.* **105**, 102029 (2009).
11. K. Maslov and L. V. Wang, "Photoacoustic imaging of biological tissue with intensity-modulated continuous-wave laser," *J. Biomed. Opt.* **13**, 024006 (2008).
12. S. Ermilov, A. Stein, A. Conjusteau, R. Gharieb, R. Lacewell, T. Miller, S. Thompson, P. Otto, B. McCorvey, T. Khamapirad, M. Leonard, and A. Oraevsky, "Detection and noninvasive diagnostics of breast cancer with two-color laser optoacoustic imaging system," *Proc. SPIE* **6437**, 643703 (2007).
13. S. Manohar, S. Vaartjes, J. Van Hespren, J. Klaase, F. Van den Engh, W. Steenbergen, and T. Van Leeuwen, "Initial results of *in vivo* non-invasive cancer imaging in the human breast using near-infrared photoacoustics," *Opt. Express* **15**, 12277 (2007).
14. G. Diebold, T. Sun, and M. Khan, "Photoacoustic monopole radiation in one, two and tree dimensions," *Phys. Rev. Lett.* **67**, 3384–3387 (1991).
15. G. Diebold and T. Sun, "Properties of photoacoustic waves in one, two and three dimensions," *Acustica* **80**, 339–351 (1994).
16. W. Star, "Diffusion theory of light transport," in *Optical-Thermal Response of Laser-Irradiated Tissue*, A. J. Welch and M. J. C. van Gemert, Eds., Plenum Press, New York (1995).
17. A. Rosencwaig, *Photoacoustics and Photoacoustic Spectroscopy*, Wiley, Hoboken, NJ (1980).
18. P. M. Morse and K. U. Ingard, *Theoretical Acoustics*, Princeton University Press, Princeton (1968).
19. American National Standard, ANSI Z136.1-2007.
20. G. Spirou, A. Oraevsky, I. A. Vitkin, and W. Whealan, "Optical and acoustic properties at 1064 nm of polyvinyl chloride-plastisol for use as a tissue phantom in biomedical optoacoustics," *Phys. Med. Biol.* **50**, N141–N153 (2005).
21. H. J. van Staveren, C. J. M. Moes, J. van Marie, S. A. Prahl, and M. J. C. van Gemert, "Light scattering in Intralipid-10% in the wavelength range of 400–1100 nm," *Appl. Opt.* **30**, 4507–4514 (1991).
22. J. Minkoff, *Signals, Noise and Adaptive Sensors: Radar, Sonar and Laser Radar*, Wiley, Hoboken, NJ (1992).
23. C. E. Cook and M. Bernfeld, *Radar Signals. An Introduction to Theory and Application*, Academic Press, New York (1967).
24. B. P. Lathi, *An Introduction to Random Signals and Communication Theory*, Scranton International Textbook Co., Scranton, PA (1968).
25. K. Maslov, G. Stoica, and L. V. Wang, "*In vivo* dark-field reflection-mode photoacoustic microscopy," *Opt. Lett.* **30**, 625–627 (2005).